Particle & Particle Systems Characterization

www.particle-journal.com

Optical Force Sensing with Cylindrical Microcontainers

Robert Meissner, Neus Oliver, and Cornelia Denz*

Quantitative force sensing reveals essential information for the study of biological systems. Forces on molecules, cells, and tissues uncover functioning conditions and pathways. To analyze such forces, spherical particles are trapped and controlled inside an optical tweezers (OT) trap. Although these spherical particles are well-established sensors in biophysics, elongated probes are envisioned for remote force sensing reducing heat damage caused by OT. There is thus a growing demand for force metrology with OT using complexly shaped objects, e.g., sac-like organelles or rod-like bacteria. Here, the employment of Zeolite-L crystals as cylindrical force sensing probes inside a single optical trap is investigated. It is shown that cylindrical objects can be used as force probes since existing calibration assays can be performed with suitable corrections. Forces of active driving assays are compared with passive calibration methods. Finally, the investigations are extended to direct force measurements based on momentum calibration, in which the influence of rotation due to torque in a single optical trap is unveiled. Simulations reveal the relation between torque and the position of equilibrium in the trap. The results highlight the functionality of Zeolite-L crystals as probes for force sensing, while opening perspectives for enhanced, accurate force metrology in biophotonics.

1. Introduction

The use of adequate probes is crucial for reliable force measurements, which reveal pivotal insights into biological processes in molecules, living cells, and tissues. Investigations on biomechanical properties of cells like elasticity have been enabled by the optical control of standard spherical probes.[1–4] Spherical probes, as isotropic objects, are easy to handle with optical tweezers and can be treated analytically. Consequently, they represent the basis for current successful techniques of force calibration.[5,6] Nevertheless, certain investigations might require the use of more complexly shaped probes. In many applications, the optical trap needs to be separated from the probed object to reduce the damaging influence of the laser beam. Spherical probes are not suited for obtaining such a separation as they are centered on the laser beam, and only allow a minimal distance between the laser beam and the probed object.[7] Moreover, most biological probes that are of utmost importance to guarantee biocompatibility of in vivo force metrology, are nonspherical objects.[8] As an example, a large group of bacteria like *Spiroplasma* or *Bacillus subtilis*, are cylindrically, spheroidal, or even helically shaped.[9,10] Endothelial cells forming the lumen of the cardiovasculature are elongated and stretched, whereas fibroblast and membrane tethers are more cylindrical or rod-like in shape.[11–14] Carbon nanotubes and Zeolite-L crystals, on the other hand, are cylindrical structures interesting for biosensing and biophotonics.[15–18] Thus, there is an increasing demand in using force probes in elongated or cylindrical shape. Whether the established methodology for force sensing based on spherical objects still applies for other geometrically anisotropic probes remains the main subject in question and motivates the present research.

The use of anisotropic probes for force sensing entails some issues to consider. A cylindrical probe will cause a resulting nonisotropic Stokes drag coefficient. As this Stokes drag coefficient is key to force calibrations in liquid media, careful calibrations in all relevant directions of motion have to be conducted. The manipulation of such probes with optical tweezers is still possible, albeit new degrees of freedom in their movement might appear. To avoid rotation due to torque, which inside a single optical trap can cover angles between 10° and 90°, previous works used two or more optical traps to manipulate cylindrical objects, placing the object laterally.[19] However, such a 2-trap configuration makes the force sensing more demanding as changes in relative position between trap and object mix between both traps, and therefore they cannot be distinguished on the detected signal.

State of the art technique in force sensing relies on active–passive calibrations with Hooke's law.[20,21] This method connects power spectral features of the Brownian motion of the trapped object with an active perturbation of the laser-particle system. As an alternative, novel direct force measurements with momentum calibration yield optical forces straight away.[6] Importantly, both calibration methods should provide similar force quantification.

For our investigations, Zeolite-L crystals are employed as force probes. Zeolite-L crystals consist of porous elongated microsized crystals featuring 1D hexagonal channels.[22] As **Figure 1** illustrates, the size among Zeolite-L crystals can manifest slight variations, but the ratio between height h and radius R is bounded and approximately constant while their

R. Meissner, Dr. N. Oliver, Prof. C. Denz
Institute of Applied Physics
University of Münster
Corrensstr. 2/4, D-48149 Münster, Germany
E-mail: n.oliver@uni-muenster.de

The ORCID identification number(s) for the author(s) of this article can be found under https://doi.org/10.1002/ppsc.201800062.

DOI: 10.1002/ppsc.201800062

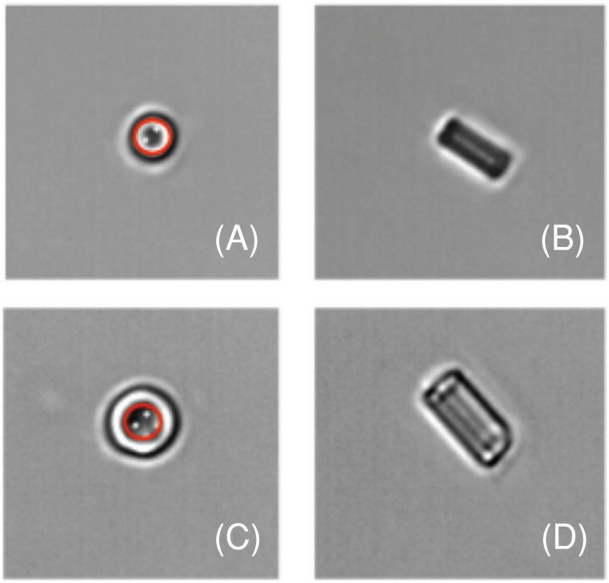

Figure 1. Snapshots of two Zeolite-L crystals inside the optical trap oriented along their (A,C) long axis, and (B,D) their corresponding untrapped lateral views. The images reveal differences in their size. The Zeolite-L crystal in panels (A) and (B) has a radius of 1.2 µm and a height of 4.2 µm while the Zeolite-L crystal in panels (C) and (D) has a radius of 2.0 µm and a height of 5.6 µm. All snapshots were acquired under the same magnification conditions.

overall shape is cylindrical. This aspect ratio is an important property for numerical simulations and measurements of cylinders inside optical traps. Current literature covers different size regimes compared to our Zeolite-L crystals.[23–26] Single-wall carbon nanotubes of aspect ratios of around 140 have been reported, as well as glass cylinders of refractive index of 1.45 with diameters either below 500 nm or above 5 µm respectively.[23–26] Our selected Zeolite-L crystals have on average an aspect ratio h/R of about 3.3 and diameters between 0.8 and 4 µm, serving as ideal test beds for optical force metrology at intermediate regimes.

Among their many applications, Zeolite-L crystals have emerged as versatile functional microcontainers, capable to host and deliver molecules into targeted living cells with an adequate transportation mechanism like optical tweezers (OT).[27,28] Their biocompatibility, cylindrical shape, and adequate dimensions make Zeolite-L crystals an ideal and simple model system to test the calibration and use of nonspherical probes in force metrology.

In this work, we calibrate a single optical trap with a cylindrical microprobe applying the power spectrum method.[21,28] Using a single optical trap, we discuss the validity of the assumptions made in the power spectrum method for nonspherical particles, focusing on the approximation for the Stokes drag coefficient. We complement our findings with comparative force simulations of spheres and cylinders in the trap that evince the relevance of the aspect ratio of the object and its imperfections. Finally, we test our calibration procedure by exerting forces to the Zeolite-L crystals and comparing our force estimation obtained from passive calibration with two other methods involving active driving: Stokes drag and direct force measurements. Our results demonstrate the feasibility of force sensing with cylindrical probes. Moreover, Zeolite-L crystals are introduced as multipurpose microprobes, which may act as containers for biomedical agents and as probes for force sensing simultaneously, representing all-in-one sensors.

2. Methods of Calibration

To trap and relocate Zeolite-L crystals and use them for force sensing we use OT. OT are a well-known tool for exerting or measuring forces in the piconewton range. Our experimental configuration includes OT with back focal plane interferometry (BFPI), which represents an adequate approach for the acquisition of data for further analysis.

2.1. Passive Calibration

One of the main uses of OT is its ability to exert or measure forces in the order of piconewtons. The trapping potential can be approximated by a harmonic potential around the equilibrium point x_0. Hence, the force is linearly related to a position displacement Δx between trapped object and optical trap via a factor called trap stiffness, κ

$$F = -\kappa \Delta x \tag{1}$$

A prerequisite for quantitative measurements with OT is a precise calibration to obtain κ of Equation (1). There are different approaches to measure forces directly or indirectly. One of the most common and reliable calibration methods to obtain κ is the so called passive calibration. Passive calibration is based on the power spectrum of the Brownian motion of the object in the trap.[21,28] The power spectrum density follows a Lorentzian function from which one can obtain the corner frequency, f_c

$$P = \frac{D}{\left(2\pi^2\right)\left(f_c^2 + f^2\right)} \tag{2}$$

This corner frequency f_c relates κ with the Stokes drag coefficient γ through

$$\kappa = 2\pi\gamma f_c \tag{3}$$

Figure 2 illustrates two power spectra from parameter estimation for a Zeolite-L crystal and a silica sphere at similar operating conditions. Although Figure 2 already demonstrates the variation in the corner frequency between both probes, the shape of the power spectra remains similar; both exhibit a plateau for low frequencies and a decay proportional to $1/f^2$ at high frequencies. The plateau is related to the localization due to the optical tweezers as the elastic trap stops motions at large amplitudes. The $1/f^2$ decay is caused by the thermal noise of Brownian motion. The frequency at which plateau and the thermal part converge is the corner frequency, see Equation (2). Having these common spectral features satisfies a first necessary condition for force measurements with

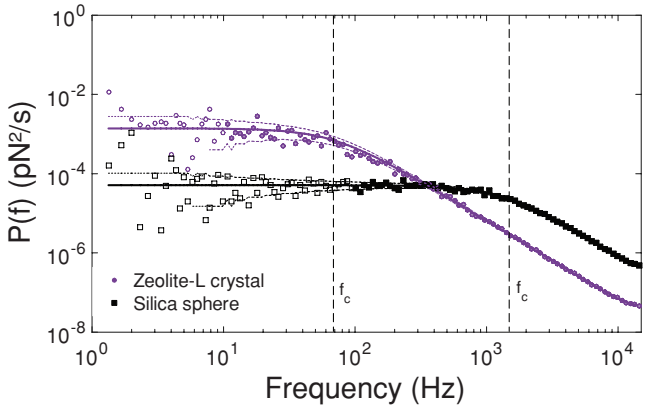

Figure 2. Power spectrum density $P(f)$ of a silica sphere of 1 µm diameter and an exemplary Zeolite-L crystal. Data not used for parameter estimation of power spectrum density are shown by empty marker symbols, data used are highlighted by filled markers. The estimated corner frequencies f_c are pointed to by dashed vertical lines. Image extracted from TweezerCalib v2.[27]

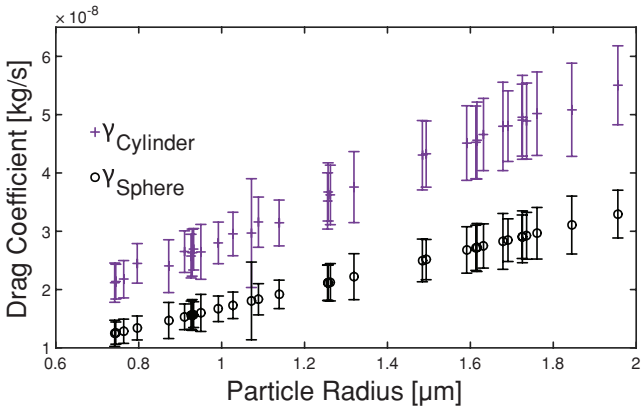

Figure 3. γ for cylinders and for spheres versus particle radius.[15,17] Both cylinders and spheres show a linear scaling with radius, although the drag coefficient values for cylinders are larger.

the microcontainers.[21] Still, to obtain the trap stiffness of the Zeolite-L crystals some assumptions on the influence of Faxen's law and drag due to their cylindrical shape need to be made.[19]

2.2. Slender Body Theory for Stokes Drag Coefficient

To obtain an accurate trap stiffness κ, a quantitative value for the drag coefficient γ is needed. The drag coefficient for a spherical particle can be theoretically determined via

$$\gamma_{\mathrm{Sph}} = 6\pi\eta R \tag{4}$$

as the viscosity of water η is known. In the case of cylindrical objects though, other approaches need to be considered. The theory of Stokes drag coefficient of thin cylindrical objects in a uniform Newtonian flow field is called Slender Body Theory.[29] It assumes forces on the cylinder acting on singular points along the long axis, therefore treating the cylinder as having a small radius compared to the height. One can derive the Stokes drag coefficient for a cylinder with its long axis parallel or orthogonal to the uniform flow. For passive calibration there is no net flow field, but the cylinder is still moving in all directions due to Brownian motion. As the cylinder is held parallel to the beam axis by its long axis, motions in the orthogonal plane are observed when driving along X direction. For trap stiffness calibration in X and Y direction we can therefore use the first term of Stokes drag coefficient orthogonal to the long axis according to Ref. [19]

$$\gamma = \frac{4\pi\eta h}{\ln\left(\frac{h}{R}\right) + \ln(2) - \frac{1}{2} - 3h/8d} \tag{5}$$

Experimental values of radius R and height h of Zeolite-L crystals at a distance d = 20 µm to the sample wall in water of viscosity η = 0.9 mPa s have been obtained by video microscopy. The $3h/8d$ fraction is the correction due to Faxen's law for the influence of the glass wall at distance d.[19] We took care of having always the same distance to the glass walls making hydrodynamic effects similar between all our experiments. Stokes drag coefficients were calculated using Equation (5). **Figure 3** shows a comparison of the calculated Stokes drag coefficient for cylinders and spheres as a function of the radius. Here, spheres were assumed to have identical radius as the cylinders to quantify the difference in trap stiffness. In the case of the cylinders, the height was also varied according to the ratio $h = 2.47R + 1.02$, which corresponds to the experimental fit to our measured crystal geometry (data not shown here). Drag coefficients increase with the particle radius for both objects. For spheres this is obvious given the linearity between γ and R shown in Equation (4); for cylinders the linearity is due to the relationship between radius R and height h, which makes Equation (5) proportional with radius. Importantly, the drag coefficients for cylinders like Zeolite-L crystals are always bigger than those for spheres. Drag coefficients can be obtained from experimental data during parameter estimation for the corner frequency, although in units of $\mathrm{pN^2\ s^{-1}}$ and therefore, they are not directly applicable. By calculating the theoretical drag coefficients based on the measured geometry, we are able to estimate trap stiffness accurately. Other aspects play a role in the calibration of cylindrical objects. In contrast to spheres, Zeolite-L crystals represent anisotropic objects that will orient along the symmetry line – or long axis – of the cylinder in the single optical trap. Therefore, we observe the trapped Zeolite-L crystals from the top. The optical forces in Z direction are relatively small due to the lateral surface as described by a schematic in **Figure 4**. Only rays which traverse through the lateral surface as well as the top or bottom faces of the cylinder will experience a relevant change in momentum ("a" beam). Effectively, the numerical aperture in the case of a cylinder is reduced. Rays of larger incident angle ("m" beam) merely cross the lateral faces. These rays behave like travelling through a plan parallel plate and are not contributing to the gradient forces. Overall, this causes a reduction in gradient forces which leads to lower trap stiffness in Z for cylinders.

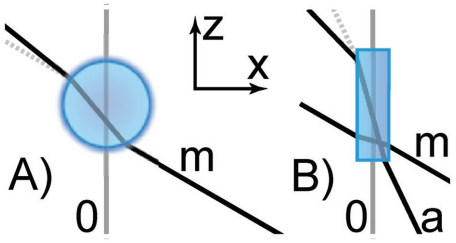

Figure 4. Schematic of ray optics describing optical forces for a sphere and a cylinder to explain the reduced numerical aperture for cylinders. A) Trapping of a sphere. The central ray parallel to the optical axis ("0" beam) does not contribute to the gradient force. The maximum angle beam defined by the numerical aperture ("m" beam) does hit the sphere surface under a nonperpendicular angle and is refracted. The angle difference before and after the sphere (between the grey dashed line and black solid line) depicts the change in light momentum. B) Trapping of a cylinder. In contrast to spheres the "m" beam hits the side wall of the cylinder and does not contribute to optical forces. Only a beam of lower numerical aperture ("a" beam) hits the bottom face of the cylinder and then the side wall causing a net change in momentum of the light.

2.3. Numerical Simulations of Cylindrical Objects inside Optical Tweezers

Simulations of optical forces for spheres and Zeolite-L crystals were conducted with the SPOT Matlab toolbox.[30] This toolbox is based on the *T*-matrix algorithm which determines the outgoing wave *P* from the incident wave *A* and the *T*-matrix of the object via[31]

$$P = TA \tag{6}$$

As both torque and optical forces are determined by differences between the incident and outgoing waves, they can be obtained by integrating over the Maxwell stress tensor for the waves calculated by Equation (6).[31] The *T*-matrix depends only on the wavelength of the light and the characteristics of the object, e.g., composition and shape. Therefore the *T*-matrix algorithm requires the computationally demanding calculation of the *T*-matrix only once. Knowing *T*, we can readily determine the final equilibrium position of the trapped object, the optical forces acting and the trap stiffness.[30] For a better understanding, we performed simulations of the optical forces in *X*- (which are analogous to *Y* due to symmetry of the applied objects) and *Z* directions as a function of their relative position to the center of the trap for spheres and cylinders. In particular, we simulated two spheres of radii 0.5 and 2 µm, and cylinders with the average Zeolite-L crystals size as well as the smallest and largest encountered sizes, see **Table 1**. Through quantitative phase contrast the refractive index of Zeolite-L crystals was found to be 1.51.[32] The refractive index of silica spheres is known from literature to be 1.45.[33] The results for an average sphere and an average Zeolite-L crystal are summarized in **Figure 5** as a function of the position with respect to the focal spot (origin). In agreement with simulations and experimental data we observe a flat force profile in *Z* direction around the equilibrium point for the cylinder.[34] Within this region the cylinder can move freely along *Z*. At positions larger than 3 µm the cylinder shows a positive force in *Z*. This positive force will accelerate the cylinder away from the trap. Taking this into consideration Zeolite-L crystals are trapped by moving the OT from the top downward onto the Zeolite-L crystal. According to Equation (1) the slope of force versus position yields the trap stiffness. We calculate the trap stiffness values in *X* and *Z* direction, see Table 1. As described by theory, the trap stiffness of a sphere is the highest if the diameter of the sphere is identical to the wavelength of the laser inside the medium.[35] Here, the ideal radius of a sphere would be 0.4 µm. Cylinders with sizes close to this radius exhibit a higher trap stiffness. The results of Table 1 also point out that the axial position of equilibrium for cylinders is shifted away from the origin in comparison to spheres. The cylinder is trapped further away from its center and more toward its bottom end. Inside a constant velocity field perpendicular to the cylinders long axis, the Zeolite-L crystal could precise and rotate around the equilibrium point.

Table 1. Trap stiffness, particle geometries, and the simulated distance of the equilibrium position along the axial direction from the focal spot of the laser beam. Values are given for a sphere of radius 500 nm, a sphere of identical diameter as the height of the mean cylinder, a mean cylinder as well as the smallest and the largest cylinder observed in the experiment.

Particle type	κ_X [arb. u.]	κ_Z [arb. u.]	Radius [µm]	Height [µm]	*Z* Equi Pos [µm]
Sphere	48	14	0.5	–	0.2
Large sphere	8	4	2	–	0.4
Small cylinder	24	8	0.8	2.9	1.5
Cylinder	17	5	1.2	4	1.2
Large cylinder	10	4	1.6	5	1.6

3. Experimental Force Measurements

From the experiments we calculated the trap stiffness in *X* and *Y* direction for our Zeolite-L crystals via Equation (3) with Equation (5), see **Figure 6**. Values for trap stiffness in *X* and *Y* direction scale proportionally. The correspondence between

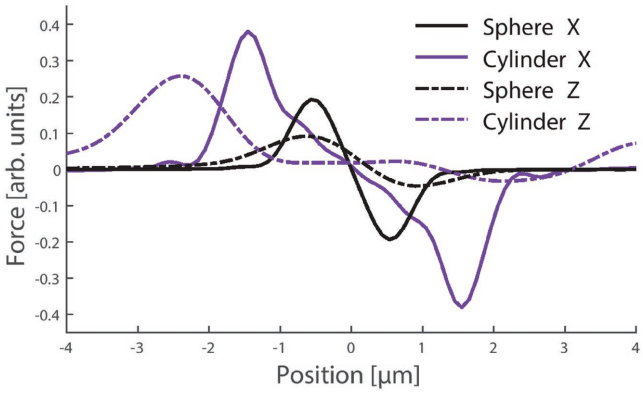

Figure 5. Simulation of the optical forces for an average cylinder (purple) and a sphere of 500 nm radius (black) along *X* (solid lines) and *Z* (dashed lines) directions. In agreement with literature, the force along the *Z* direction of the cylinder shows a plateau causing a free motion within this region.[33] Final positions along the *Z* direction are summarized in Table 1.

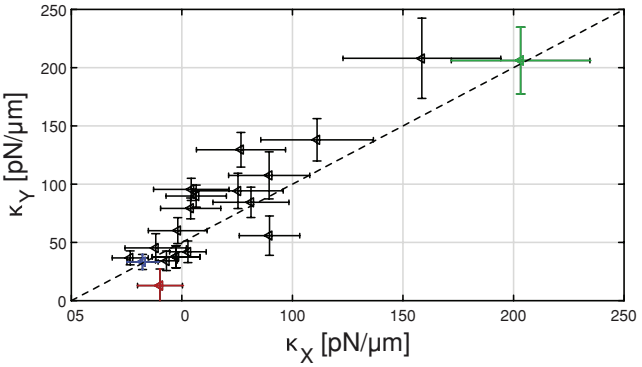

Figure 6. Trap stiffness of Zeolite-L crystals in *X* and *Y* direction. The dashed line is the unity line. The two Zeolite-L crystals with stiffness above 150 pN μm^{-1} are two examples of large Zeolite-L crystals with defects comparable to those of the Zeolite-L crystal in Figure 1c,d. All measurements were done at similar laser power. Three Zeolite-L crystals are highlighted. The Zeolite-L crystal from Figure 1a is shown in blue, the one from Figure 1c is shown in green. A Zeolite-L crystal with an elliptical base is highlighted in red.

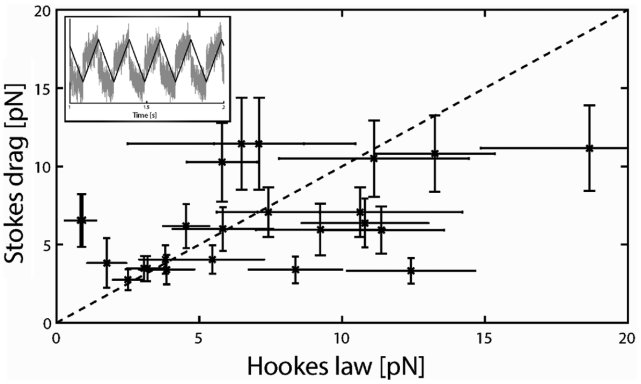

Figure 7. Comparison of force due to Hooke's law with Stokes drag. The dashed line is the unity line. The inset shows the triangular drive signal (black) and the measured position signal (grey) over time.

trap stiffness in *X* and *Y* confirms the equivalence of both directions for Zeolite-L crystals, and the validity of the calibration method for subsequent force measurements. The Zeolite-L crystal with lowest trap stiffness, coloured in blue in Figure 6, is shown in Figure 1a,b. It displays a perfect cylindrical shape and it is also the smallest Zeolite-L crystal. The longest observed Zeolite-L crystal has one of the largest trap stiffness, is shown in Figure 1c,d and is coloured in green in Figure 6. It exhibits shape imperfections. We observed that Zeolite-L crystals with large trap stiffness tend to display such imperfections in shape, whereas Zeolite-L crystals of perfect cylindrical shape have small trap stiffness. As our schematic discussion of shape in Figure 4 describes, a perfect cylinder should have a reduced effective numerical aperture causing reduced optical forces. Imperfections in shape will refract the light differently, causing a smaller reduction in effective numerical aperture, larger optical forces and, in turn, larger trap stiffness. The Zeolite-L crystal with the smallest trap stiffness in *Y* direction has an elliptical instead of a circular base, which explains the anisotropy in trap stiffness along *X* and *Y* direction, see Figure 6 red value. In analogy to Ref. [15] we tested for dependence on the *X*–*Y* orientation of the linear polarization, but found no significant dependence or precession around the long axis (data not shown here).

We next tested the validity of the passive calibration procedure with active calibration assays. We exerted forces on the object by driving the sample with a triangular position motion.[19] The triangular position motion gives regimes of constant velocity, which correspond to constant displacements and optical forces due to the acting Stokes drag $F = \gamma v$. We calculate the Stokes drag from the applied stage velocity v and compare with the passive calibration results via Equation (1), see **Figure 7**. The inset shows the experimentally observed position data (grey line) together with the applied triangular stage motion (blackline). At constant velocity the measured force is approximately constant. The data points illustrate agreement between the calculated Stokes drag and passive calibration. The large error bars are due to limitations in the determination of the displacement by camera, the uncertainties of the Stokes drag coefficient and fluctuations in the driving velocity of the stage. The results confirm the possibility to use passive calibration methods such as power spectrum method with cylinders. Though both active and passive results depend on the Stokes drag coefficient γ, they do point out that our determinations of stage velocity, particle displacement and especially trap stiffness agree.

To overcome this dependence on γ, we completed our investigations acquiring an independent and direct reading of the applied optical forces, also known as direct force measurement. It is an improved kind of BFPI based on the so-called momentum calibration, which obtains all the forward scattered light from the trapped particle. The technique is able to calculate the change in light momentum due to the momentum transfer from light to the particle.[6] This momentum calibration is independent of the object and the applied light field.[6,19,36] We compare the direct force measurements with forces derived from Equation (1) in **Figure 8**. We observe many Zeolite-L crystals to show a relevant agreement between the direct forces and the

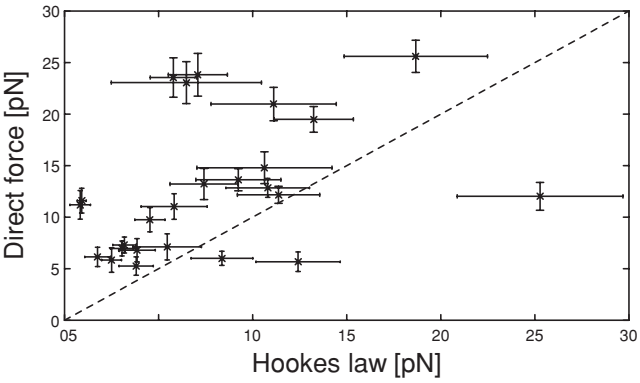

Figure 8. Comparison of forces due to Hooke's law from passive calibration with direct forces. Results from direct force measurements are shifted toward larger values than those determined by Hooke's law. However, the values remain distributed close to the unity line. These results illustrate a good experimental agreement, given that factors like shape irregularities, underestimated Stokes drag coefficient, and additional optical forces due to torque can jeopardize the correspondence.

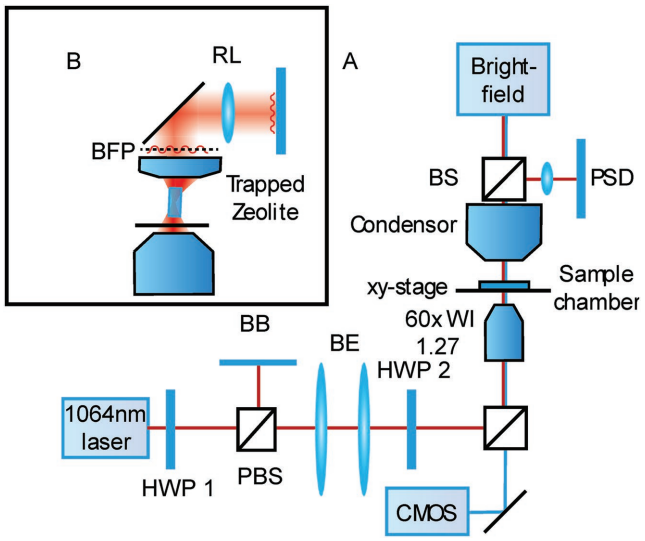

Figure 9. A) Schematic OT system used for steering Zeolite-L crystals. B) Close up of sample plane and back focal plane interferometry with trapped Zeolite-L crystal. HWP: Half-wave plate, PBS: polarizing beam splitter, BB: beam blocker, BE: beam expansion, BS: beam splitter, WI: Water immersion objective, PSD: position sensitive detector, BFP: Back focal plane, RL: relay lens, CMOS: conjugate metal oxide semiconductor camera.

forces from Equation (1), although a bias toward larger direct forces is observed. We find three prime sources of differences: the shape irregularities of some Zeolite-L crystals, an underestimated Stokes drag coefficient, and torque forces.

Zeolite-L crystals do have significant differences in shape among them, see Figure 1. Some of them clearly show a hexagonal base shape, others have a more circular appearance, and even others show missing corners or edges. The hexagonal base shape will lead to an increased beam waist and thus reduced gradient forces as rays are not focused at the same position anymore. Our simulations cannot take this hexagonal shape into account but key differences between spherical and cylindrical objects should be simulated correctly. Experiments show that Stokes drag forces are identical to direct forces if cylinders are held by two optical traps and actively driven.[19] This arrangement minimizes precession of the cylinder around the long axis reducing torque. In our case, we grab the Zeolite-L crystal with a single trap, which in principle allows pitch, yaw, and roll around all three axes. It is experimentally difficult with our current system to distinguish torque in our force measurements.

As illustrated by the simulations (Figure 5, Table 1), Zeolite-L crystals are not held at their centre along the optical axis but closer to the bottom of the crystal, and the single optical trap barely limits both precession and pitch and yaw rotation. During driving; Stokes drag forces cause a pitching motion of the Zeolite-L crystal. Consequently, a net change in angle of forward scattered light occurs, increasing the measured force. This increase in force due to pitch is not taken into account by the method of passive force calibration applied here, direct force measurement, however, do. If the cylinder is moved slowly then the exerted torques should be minor, e.g., when pushing the Zeolite-L crystal vertically onto a surface or cell membrane. Our determination of torque angle by video microscopy of the projected shape of the hexagonal base is accurate to a few degrees, and within this accuracy, we determined stable torque angles not greater than 3°. The increased refractive index should lead to higher optical forces and thus stronger confinement of the cylinder inside the optical trap. As a result, rotation of the Zeolite-L crystal inside the optical trap is restricted, causing a reduction in achievable torque angles.

An important aspect to consider is the applicability of Slender Body Theory, which relies on the height of the object being much larger than its radius.[29] Literature until now offers expansions to higher orders for ratios $h/R > 4.6$, indicating again that our microcontainers belong to a different range that requires additional corrections. Improvements to the Stokes drag coefficient would keep Figure 7 similar, only scaling values along the unity line. However, the corrections should significantly improve the correspondence in Figure 8 with an increase of values of Hooke's law from Equation (1) resolving the current shortcomings in agreement. We expect a better concordance between direct forces and forces due to Equation (1) if further improvements on the quantification of torque on cylinders in optical tweezers and the Stokes drag coefficients are carried out. As all these major influences should contribute to the direct measured forces, the found consensus between direct forces and forces calculated using Equation (1) can be considered as good.

4. Conclusion

We employed microcontainers of cylindrical shape, Zeolite-L crystals, for the experimental calibration of optical forces. Our Zeolite-L crystals possess the advantages of being compatible for biological applications and have intermediate aspect ratios that were missing in force sensing investigations up to now. The Zeolite-L crystals show increased Stokes drag coefficients but reduced trap stiffness in both experiments and simulations in comparison to standard used silica spheres. Passive calibration of cylindrical probes was successfully performed, obtaining expected power spectrum features, as well as similar trap stiffness values in X and Y directions. Active driving was used to create additional references to back up our hypothesis of the applicability of Zeolite-L crystals as force probes. We found a good agreement between theoretically expected Stokes drag force and the experimentally measured forces according to Hooke's law. As both forces are depending on the applied theory for Stokes drag coefficient, incorporating higher-order terms of h/R should not change its validity.[29] The comparison of the forces from passive calibration due to Hooke's law with direct force measurements show a remarkable yet weaker agreement, which can be attributed to shape irregularities, underestimated Stokes drag coefficient and torque. Nevertheless, our derivations of torque indicate that the precession angles are too small to have a strong influence on the optical forces. Further investigations should include higher orders of the series expansion of the Slender-Body theory, together with more sophisticated techniques to confirm pitch and precession of trapped particles. Despite all these additional contributions to the optical force, we show that proper trap calibration with Zeolite-L

crystals is achieved. Our results show, on the one hand, the legitimacy of state-of-the-art power spectrum method based calibrations of optical tweezers in the context of cylindrical objects. On the other hand, we demonstrate the applicability of the Zeolite-L containers as force sensors using a single optical trap configuration. Furthermore, the viability of cylinders to determine forces, e.g., during delivery of drugs onto cell membranes or when deforming cells is foreseen. We expect our findings to open new pathways toward calibration of force probes possessing irregular asymmetric shapes, such as red blood cells or diatoms.[37,38]

5. Experimental Section

The system for the optical tweezers is based on a tightly focused laser beam used in combination with a lens of high numerical aperture. The optical trap was generated at the equilibrium point between the gradient forces and the scattering forces.[39] For the subsequent passive calibration analysis, the acquisition of position data of the trapped object at kilohertz rate over several seconds was required.[21,40] The change in momentum of the transmitted laser beam was observed by imaging the interference of scattered and unscattered light in the back focal plane of the condensor lens. As scattered light will propagate under a different angle compared to the unscattered light, there will be a shift in light fields in the back focal plane causing an interference.[41] The method was stable against changes in position of the object and precise with resolutions of nanometres and microseconds.[41]

A schematic of the system is shown in **Figure 9**. The laser was a continuous-wave diode-pumped solid-state laser (Cobolt Rumba, Sweden) operating at 1064 nm with a single mode output (Gaussian TEM00 mode) and maximum output power of 3 W. A half-wave plate (HWP1) and polarizing beam splitter (PBS) permitted regulation of intensity in the trapping plane. Two lenses expanded the beam while a second half-wave plate (HWP2) was placed in the setup only for polarization-related investigations. The beam was imaged onto the back focal plane of the trapping objective. The objective was a water-immersion 60× with a NA of 1.27 built into a Nikon Ti-E 2000 microscope. A Lunam T-40i (Impetux Optics, Spain) was used for BFPI and direct force measurements. Active driving experiments were performed by a home-made piezo stage with a maximum amplitude of 3 µm driven by a function generator (Agilent Technologies, USA). Brightfield images were acquired by a USB3 uEye 3376-CP camera (IDS Imaging Development Systems, Germany) to determine particle position during active driving. Particle tracking algorithms were based on optimized Center of Mass algorithms.[42,43] Power spectrum method calibration was done with TweezerCalib v2.[44] Zeolite-L crystals were kindly supplied by Studer and Buscher from the University of Muenster, whereas the silica spheres of 1 µm in diameter were obtained from Kisker Biotech, Germany and dissolved in ultra pure water.

Acknowledgements

R.M. and N.O. have contributed equally to this work. This work was partially supported by the Deutsche Forschungsgemeinschaft (DFG) Cells-in-Motion Cluster of Excellence (EXC1003-CIM), and the University of Muenster, Germany.

Conflict of Interest

The authors declare no conflict of interest.

Keywords

biophysics, force sensing, momentum calibration, optical tweezers, power spectrum method

Received: February 13, 2018
Revised: March 7, 2018
Published online:

[1] B. H. Blehm, A. Devine, J. R. Staunton, K. Tanner, *Biomaterials* **2015**, *83*, 66.
[2] F. Hoerner, R. Meissner, S. Polali, J. Pfeiffer, T. Betz, C. Denz, E. Raz, *J. Biophotonics* **2017**, *10*, 1.
[3] S. Fusco, P. Memmolo, L. Miccio, F. Merola, M. Mugnano, A. Paciello, P. Ferraro, P. A. Netti, *RSC Adv.* **2016**, *6*, 24245.
[4] F. Merola, Á. Barroso, L. Miccio, P. Memmolo, M. Mugnano, P. Ferraro, C. Denz, *Cytometry, Part A* **2017**, *91*, 527.
[5] I. M. TolićNørrelykke, K. Berg-Sørensen, H. Flyvbjerg, *Comput. Phys. Commun.* **2004**, *159*, 225.
[6] A. Farré, M. Montes-Usategui, *Opt. Express* **2010**, *18*, 11955.
[7] S. Raj, M. Wojdyla, D. Petrov, *Biomed. Opt. Express* **2012**, *3*, 753.
[8] G. R. Kirkham, E. Britchford, T. Upton, J. Ware, G. M. Gibson, Y. Devaud, M. Ehrbar, M. Padgett, S. Allen, L. D. Buttery, K. Shakesheff, *Sci. Rep.* **2015**, *5*, 1.
[9] M. Koch, A. Rohrbach, *Nat. Photonics* **2012**, *6*, 680.
[10] B. Kemper, Á. Barroso, M. Woerdemann, L. Dewenter, A. Vollmer, R. Schubert, A. Mellmann, G. v. Bally, C. Denz, *J. Biophotonics* **2013**, *6*, 260.
[11] W. W. Sugden, R. Meissner, T. Aegerter-Wilmsen, R. Tsaryk, E. V. Leonard, J. Bussmann, M. J. Hamm, W. Herzog, Y. Jin, L. Jakobsson, C. Denz, A. F. Siekmann, *Nat. Cell Biol.* **2017**, *19*, 653.
[12] B. Pontes, N. B. Viana, L. T. Salgado, M. Farina, V. Moura Neto, H. M. Nussenzveig, *Biophys. J.* **2011**, *101*, 43.
[13] J. T. Zahn, I. Louban, S. Jungbauer, M. Bissinger, D. Kaufmann, R. Kemkemer, J. P. Spatz, *Small* **2011**, *7*, 1480.
[14] S. Baoukina, S. J. Marrink, D. P. Tieleman, *Biophys. J.* **2012**, *102*, 1866.
[15] J. Zhang, H. I. Kim, C. H. Oh, X. Sun, H. Lee, *Appl. Phys. Lett.* **2006**, *88*, 053123.
[16] Á. Barroso, K. Dieckmann, C. Alpmann, T. Buscher, A. Studer, C. Denz, *SPIE OPTO* **2015**, *93790U*, 93790U.
[17] B. Nermin, S. Kehr, K. Riehemann, J. El-gindi, A. Schaefer, H. Fuchs, H. J Galla, L. De Cola, *Adv. Funct. Mater.* **2010**, *20*, 2248.
[18] N. Wong, S. Kam, M. O' Connell, J. A. Wisdom, H. Dai, *Proc. Natl. Acad. Sci. USA* **2005**, *102*, 11600.
[19] F. Catala, F. Marsà, M. Montes-Usategui, A. Farré, E. Martín-Badosa, *Sci. Rep.* **2017**, *7*, 42960.
[20] M. Fischer, A. C. Richardson, S. Nader S. Reihani, L. B. Oddershede, K. Berg-Sørensen, *Rev. Sci. Instrum.* **2010**, *81*, 015103.
[21] K. Berg-Sørensen, H. Flyvbjerg, *Rev. Sci. Instrum.* **2004**, *75*, 594.
[22] G. Calzaferri, D. Brühwiler, S. Megelski, M. Pfenniger, M. Pauchard, B. Hennessy, H. Maas, A. Devaux, U. Graf, *Solid State Sci.* **2000**, *2*, 421.
[23] Y. Cao, A. B. Stilgoe, L. Chen, T. A. Nieminen, *Opt. Express* **2012**, *20*, 3077.
[24] R. C. Gauthier, *J. Opt. Soc. Am. B* **1997**, *14*, 3323.
[25] O. M. Maragò, P. H. Jones, F. Bonaccorso, V. Scardaci, P. G. Gucciardi, A. G. Rozhin, A. C. Ferrari, *Nano Lett.* **2008**, *8*, 3211.
[26] R. C. Gauthier, M. Ashman, C. P. Grover, *Appl. Opt.* **1999**, *38*, 4861.
[27] Á. Barroso, K. Dieckmann, C. Alpmann, T. Buscher, A. Studer, C. Denz, *Proc. SPIE* **2015**, *9379*, 1.
[28] Y. Jun, S. K. Tripathy, B. R. J. Narayanareddy, M. K. Mattson-Hoss, S. P. Gross, *Biophys. J.* **2014**, *107*, 1474.
[29] J. B. Keller, S. I. Rubinow, *J. Fluid Mech.* **1976**, *75*, 705.

[30] M. A. Taylor, *Sci. Rep.* **2017**, *7*, 555.
[31] T. A. Nieminen, V. L. Y. Loke, A. B. Stilgoe, G. Knöner, A. M. Brańczyk, N. R. Heckenberg, H. Rubinsztein-Dunlop, *J. Opt. A: Pure Appl. Opt.* **2007**, *9*, S196.
[32] P. Runde, *Master Thesis*, University of Muenster **2017**.
[33] C. G. Hebert, S. Hart, T. A. Leski, A. Terray, Q. Lu, *Anal. Chem.* **2017**, *89*, 10296.
[34] D. B. Phillips, M. J. Padgett, S. Hanna, Y.-L. D. Ho, D. M. Carberry, M. J. Miles, S. H. Simpson, *Nat. Photonics* **2014**, *8*, 400.
[35] R. S. Dutra, N. B. Viana, P. A. Maia Neto, H. M. Nussenzveig, *Phys. Rev. A* **2014**, *90*, 013825.
[36] A. Farré, F. Marsà, M. Montes-Usategui, *Opt. Express* **2012**, *20*, 12270.
[37] P. L. Johansen, F. Fenaroli, L. Evensen, G. Griffiths, G. Koster, *Nat. Commun.* **2016**, *7*, 1.
[38] S. N. Olof, J. A. Grieve, D. B. Phillips, H. Rosenkranz, M. L. Yallop, M. J. Miles, A. J. Patil, S. Mann, D. M. Carberry, *Nano Lett.* **2012**, *12*, 6018.
[39] A. Ashkin, J. M. Dziedzic, J. E. Bjorkholm, S. Chu, *Opt. Lett.* **1986**, *11*, 288.
[40] M. Andersson, F. Czerwinski, L. B. Oddershede, *J. Opt.* **2011**, *13*, 044020.
[41] F. Gittes, C. F. Schmidt, *Opt. Lett.* **1998**, *23*, 7.
[42] J. C. Crocker, D. G. Grier, *J. Colloid Interface Sci.* **1996**, *179*, 298.
[43] N. Chenouard, I. Smal, F. d. Chaumont, M. Maška, I. F. Sbalzarini, Y. Gong, J. Cardinale, C. Carthel, S. Coraluppi, M. Winter, A. R. Cohen, W. J. Godinez, K. Rohr, Y. Kalaidzidis, L. Liang, J. Duncan, H. Shen, Y. Xu, K. E. G. Magnusson, J. Jaldén, H. M. Blau, P. Paul-Gilloteaux, P. Roudot, C. Kervrann, F. Waharte, J. Y. Tinevez, S. L. Shorte, J. Willemse, K. Celler, G. P. v. Wezel, H. Dan, Y. Tsai, C. Ortiz de Solórzano, J. C. Olivo-Marin, E. Meijering, *Nat. Methods* **2014**, *11*, 281.
[44] P. M. Hansen, I. M. Tolic-Nørrelykke, H. Flyvbjerg, K. Berg-Sørensen, *Comput. Phys. Commun.* **2006**, *175*, 572.

